RSC Advances

PAPER

View Article Online
View Journal | View Issue

Cite this: *RSC Adv.*, 2020, **10**, 38505

Engineering of zeolite BEA crystal size and morphology *via* seed-directed steam assisted conversion†

Tatiana O. Bok,[a] Egor P. Andriako,[a] Elena E. Knyazeva[ab] and Irina I. Ivanova*[ab]

The mechanism of seeding of zeolite BEA *via* steam assisted conversion has been studied using BEA seeds with different composition. The catalysts are characterized by X-ray diffraction, scanning and transmission electron microscopy, nitrogen adsorption–desorption, Hg-porosimetry, X-ray fluorescence and TPD of ammonia, and evaluated in benzene alkylation with propene. The results show that variation of the SiO_2/Al_2O_3 ratio from 25 to 250 in BEA seeds changes the mechanism of seeding from "core–shell" to a "dissolution" mechanism, which can serve as a tool for engineering the morphological, textural and catalytic properties of BEA zeolites. Al-rich seeds (SiO_2/Al_2O_3 = 25) do not dissolve during gel preparation and initiate dense oriented crystal growth on their surface resulting in the formation of large polycrystals (1–2 μm) with ordered densely intergrown nanocrystallites. In contrast, Si-rich seeds (SiO_2/Al_2O_3 = 250) dissolve into tiny fragments, which serve as individual nuclei leading to formation of tiny isolated nanocrystallites aggregated into small hierarchical aggregates with high intercrystalline mesoporosity. The decrease of particle size and formation of intercrystalline mesoporosity in hierarchical aggregates improves the accessibility of acidic sites and facilitates the diffusion of reaction products, which leads to the significant improvement of catalytic activity and reduces the deactivation resulting in higher stability with time on stream in cumene synthesis from benzene and propylene.

Received 5th September 2020
Accepted 12th October 2020

DOI: 10.1039/d0ra07610d

rsc.li/rsc-advances

Introduction

BEA zeolite is among the most widely used zeolites. It exhibits a three-dimensional pore system formed by 12-membered ring channels with a diameter of 0.76 × 0.64 and 0.55 × 0.55 nm, which ensures good accessibility of acid sites, high thermal stability and high acidity. Due to these properties BEA zeolite is an excellent catalyst and sorbent for a broad range of industrial processes[1] including alkylation and hydroalkylation of aromatics,[2,3] alkanes alkylation,[4] transalkylation of alkylaromatics,[5] Friedel–Crafts acylation,[6] catalytic cracking[7] and depollution/decontamination processes (SCR of NO_x, VOC adsorption).[8] In addition, it shows high potential for the transformation and valorisation of bio-sourced substrates.[9] It is well known that BEA zeolite can be obtained in the form of individual crystals (including nanocrystals),[10,11] polycrystals with intergrown nanocrystallites[12] and hierarchical aggregates of nanocrystals with high content of intercrystallite mesopores.[11,13,14] However, there is a lack of information on the means to control these morphological features and on their effect on the catalytic performance of BEA catalysts.

The conventional method of BEA zeolite synthesis involves hydrothermal crystallization of alkaline silico-alumina reaction mixtures with high concentration of organic structure-directing agent (OSDA) ($OSDA/SiO_2$ = 0.4–0.6) at elevated temperatures (130–150 °C) and autogenous pressure.[15,16] The most used OSDA for the formation of BEA zeolite is tetraethylammonium (TEA) cation, which is applied in the form of hydroxide or halides. High content of TEA in the reaction mixture is necessary for the creation of high concentration of zeolitic nuclei and maintaining highly alkaline pH of synthesis. However, the cost of TEA is rather high and constitutes the main contribution to the production cost of BEA zeolite. Besides that, the removal of TEA from zeolitic porous system requires calcination, which gives rise to high energy consumption, high environmental burden, the necessity of processing of the waste gas and water produced by this process and therefore further increases the production costs.

To decrease the cost of BEA zeolite synthesis the OSDA-free route has been proposed. Xiao and co-workers reported an OSDA-free method in the presence of calcined BEA seeds.[17] Majano *et al.* pointed that non-calcined seeds are preferable for

[a]*A. V. Topchiev Institute of Petrochemical Synthesis, Russian Academy of Sciences, Laboratory No. 5, Leninskiy Prospect 29, 119991 Moscow, Russia. E-mail: ivanova_ii@ips.ac.ru; Tel: +7-495-647-5927 extn 254*

[b]*Department of Chemistry, Lomonosov Moscow State University, Leninskie Gory 1, Bld.3, 119991 Moscow, Russia. E-mail: iiivanova@phys.chem.msu.ru; Fax: +7-495-932-8846; Tel: +7-495-939-3570*

† Electronic supplementary information (ESI) available: Experimental XRD; BJH pore size distribution; FT-IR spectra and ^{29}Si MAS NMR spectra of BEA seed crystals, calculations the amount of defects in seeds; calculation of the amount of crystals in seeds and products. See DOI: 10.1039/d0ra07610d

seed-assisted synthesis.[18] Kamimura *et al.* suggested to use OSDA-free BEA as renewable seed crystals for the synthesis of completely "green beta".[19] The development of OSDA-free seed-assisted synthesis was a significant step forward towards industrial production of BEA zeolite,[20] however this route can be used only for the synthesis of low silica BEA zeolites (SiO_2/Al_2O_3 < 15)[19] with rather large crystal size (>400 nm).[21]

Another breakthrough in the field of BEA zeolite synthesis was related to the development of steam assisted conversion (SAC) method.[22,23] This method involves crystallization of dry silico-alumina gel containing non-volatile SDA in the presence of steam. It allows significantly reduce the amount of template and water in the initial reaction mixture and therefore decrease the amount of waste, as well as increase the yield of the solid phase because of almost complete incorporation of reagents from the initial gel into the zeolite. Besides that, SAC method makes possible to obtain BEA zeolites with broad range of Si/Al ratio within 7 to ∞.[24,25] Moreover, under proper conditions of synthesis this method can yield hierarchical zeolites composed of tiny nanocrystals assembled in aggregates containing large content of intercrystalline mesopores responsible for better intercrystallite diffusion and higher accessibility of zeolitic micropores.[13] However, the latter result can be achieved in the presence of rather large amounts of template ($TEAOH/SiO_2$ > 0.425).

To reduce further the amount of template and to decrease the crystallization temperature and time, Cheng *et al.*[14] proposed to combine SAC and seeding technologies and established low-seeded low-templated seeding-steam-assisted conversion (SSAC) method benefiting from synergetic action of TEOH and beta seeds. They have found that the optimal amount of seeds is 1% and the optimal $TEAOH/SiO_2$ ratio is 0.1. Under these conditions, nanosized zeolite BEA with high crystallinity and abundant mesoporosity can be obtained. However, no information is available on the nature of seeds required for this process as well as on the mechanism of seeding operating during the steam assisted conversion. Herein, we report on the role of BEA seeds with different composition in the synthesis of zeolite BEA *via* SSAC method. We show that the composition of seeds is crucial for the mechanism of seeding and can serve for engineering of BEA crystal size and morphology. Furthermore, we demonstrate that it is of high importance for BEA catalytic performance in cumene synthesis from benzene and propene, which is among the most important areas of BEA zeolite applications.[26–29]

Experimental

Synthesis of BEA zeolites

The initial gel was prepared according to the procedure.[14] Sodium hydroxide NaOH (98%, Alfa Aesar) was dissolved in distilled water, then aluminum sulfate $Al_2(SO_4)_3 \cdot 18H_2O$ (Alfa Aesar) was added. After dissolving the salt, TEAOH (35% aqueous solution, Aldrich), seed crystals of BEA zeolite (SiO_2/Al_2O_3 = 25, 75, 250, Zeolyst) and Aerosil were added stepwise and the resulting mixture was mechanically mixed until the homogeneous state. The amount of seeds was 1 wt% from the amount SiO_2 in the gel. The reaction mixture had the following composition: $Al_2O_3 \cdot 43.6SiO_2 \cdot 9.1Na_2O \cdot 4.4TEAOH \cdot 350H_2O \cdot$(1% seed). The resulting gel was dried for 12 hours at a temperature of 60 °C and poured onto a holder in an autoclave containing some water at the bottom. The crystallization was conducted at 140 °C for 48 hours. For comparison, one synthesis was carried out without seeds. In the latter case, the crystallization time was 120 hours. The samples are denoted as BEA-s-*X*, where *X* is SAR (25, 75, 250) of BEA seeds, added to initial gel. The sample denoted as BEA corresponds to the crystallization of dry gel prepared without seeds.

Upon the completion of crystallization, the solid product was separated on a Sigma-6-16 centrifuge at a rotor speed of 8000 rpm for 10 min. The crystalline product was washed to pH ~ 9, dried at 60 °C for 12 h, and calcined in an air flow at 550 °C for 10 h (heating rate was 2 °C min^{-1}).

To obtain the H-form of BEA zeolites, samples were ion exchanged in 0.1 mol L^{-1} NH_4NO_3 solution thrice at 80 °C for 3 h. After ion exchange, the solid phase was washed with distilled water, dried at a temperature of 100 °C for 12 hours, and then calcined in a furnace in a constant stream of air at 500 °C for 6 hours.

Characterization

X-ray phase analysis (XRD) of the samples was performed using diffraction patterns obtained on a Bruker D2PHASER X-ray diffractometer (radiation CuKα). The diffraction patterns were recorded in the 2θ angle range of 5–50° with a step of 0.05°, a slit width of 1 mm, and a recording time per point of 3. The degree of crystallinity of the samples was calculated relative to the external standard (highly crystalline BEA sample) using the reflection at *ca.* 23 degrees.

The chemical composition of crystallization products isolated at different steps of the synthesis was determined using the X-ray fluorescence analysis method on a Thermo Scientific ARL Perform'X instrument with a 3.5 kW rhodium tube.

Scanning electron microscopy (SEM) images of the samples were obtained on a Hitachi TM3030 scanning electron microscope. Before imaging, the samples were covered with gold by vacuum deposition. Transmission electron microscopy (TEM) images were recorded on a transmission electron microscope FEI Osiris 300 (kV) with EDS Bruker SuperX operated at 200 kV, using TEM and HAADF detector.

The pore structure of the samples was studied by low-temperature nitrogen adsorption–desorption and mercury porosimetry. Low-temperature nitrogen adsorption isotherms were recorded on a Micromeritics ASAP 2010 porosimeter. Specific surface area and the volume of micropores (with a diameter less than 2 nm according to the IUPAC classification) were determined by the t-plot method. The volume of mesopores with the size of 2–50 nm was determined by the Barrett–Joyner–Halenda (BJH) method. The macropore volume was determined on a Micromeritics AutoPore 9605 mercury porosimeter in accordance with the volume of mercury absorbed by the sample macropores with a diameter of more than 50 nm.

The acidic properties of the samples were studied by temperature-programmed desorption of ammonia (NH_3–TPD).

Experiments were conducted on a USGA-101 chemisorption analyzer (UNISIT, Russia). The sample in an amount of 0.15–0.20 g was charged into a quartz tube reactor; the standard automatic pretreatment included the following sequential procedures: calcining the sample in a helium flow at 500 °C for 1 h, saturation with ammonia at 60 °C for 15 min and removal of physically adsorbed ammonia in a helium flow at 100 °C. The NH_3–TPD experiment was conducted in a helium flow (30 mL min^{-1}) at a rate of temperature increase of 8 °C min^{-1}; desorbed ammonia was registered using a thermal conductivity detector. The content of acid sites (a_0, μmol g^{-1}) was calculated basing on the amount of ammonia desorbed from the catalyst surface in the temperature range within 100–700 °C.

Catalytic testing

The catalytic properties of the samples were studied in benzene alkylation with propylene in a continuous flow catalytic unit equipped with a fixed-bed reactor under 3 MPa, at 170 °C, WHSV of 52 and 2.4 h^{-1} (referred to the propylene), in a nitrogen flow of 30 mL min^{-1}, and a benzene/propylene molar ratio of 5/1 and 10/1. A weighed portion of the catalyst with a fraction of 0.5–1 mm diluted with quartz was loaded into the reactor. The temperature of the reaction zone was controlled using a chromel–alumel thermocouple located in the catalyst bed. A benzene–propylene mixture was fed into the reactor by means of a piston pump. Prior to the reaction, all the catalysts were pre-treated at 350 °C in a nitrogen flow of 30 mL min^{-1} for 30 min; after that, the temperature was decreased to the reaction temperature.

Gaseous and liquid reaction products were analyzed on Crystal-2000M chromatograph (Chromatec Analytic) equipped with flame ionization detectors using quartz capillary columns coated with the SE-30 phase (30 m). Nitrogen was used as a carrier gas.

Results and discussion

Structural, textural and morphological properties of the samples

To clarify the role of the chemical composition of seeds in SSAC synthesis of BEA, three BEA samples with SiO_2/Al_2O_3 ratio (SAR) of 25, 75 and 250 purchased from ZEOLYST were used as seeds. The synthesis was performed from dry gels with the same template content (the TEAOH/SiO_2 molar ratio of 0.1) and the same seed amount (1 wt%) using the procedure described previously.[22] It should be noted that the size of BEA seeds with SAR of 25 and 75 was similar (100–300 nm), while the size of BEA crystals with SAR of 250 was larger (0.4–1.3 μm) (Fig. 1). The possibility to obtain BEA zeolite without seeds under the same conditions was also studied. Table 1 shows the inorganic yield of products obtained after separation and washing, their chemical composition, textural and morphological properties.

According to XRD data (Fig. 2), the crystallization of seeded dry gels for 48 h at 140 °C gives highly crystalline BEA zeolites. Reflections corresponding to other crystalline or amorphous phases are not detected. On the contrary, the crystallization of the dry gel in the absence BEA seeds at this low template amount leads to amorphous material. Only at longer crystallization times (120 h) XRD pattern shows the reflections of zeolite

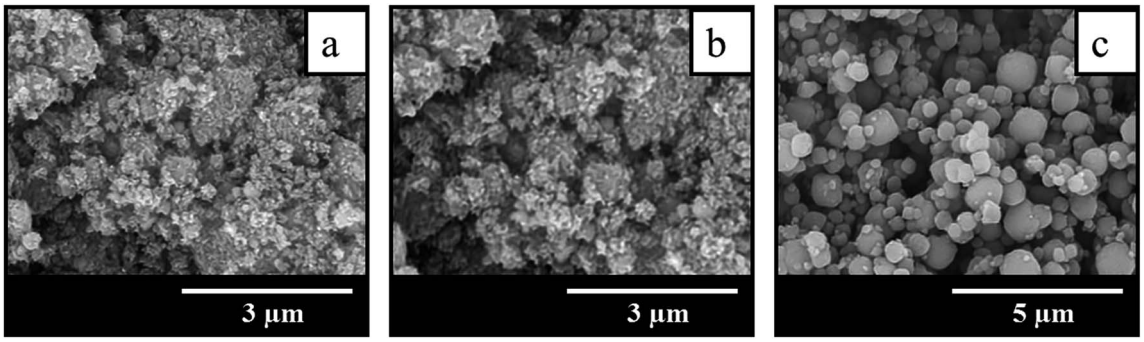

Fig. 1 SEM images of the BEA seed crystals with different SAR: (a) 25; (b) 75; (c) 250.

Table 1 Characteristics of the samples

Samples	SiO_2/Al_2O_3 molar ratio			Textural characteristics			Inorganic yield, %	Degree of crystallinity, %	$a_0(NH_3)$, μmol g^{-1}	Crystal size, μm
	In seeds	In initial gel	In product	S_{BET}, m^2 g^{-1}	V_{total}, cm^3 g^{-1}	V_{micro}, cm^3 g^{-1}				
BEA	—	44	39	520	0.28	0.21	89	69	770	1.5–4.0
BEA-s-25	25	44	37	500	0.29	0.20	88	82	795	0.7–1.4
BEA-s-75	75	44	35	530	0.38	0.20	86	80	805	0.3–1.3
BEA-s-250	250	44	32	625	0.47	0.24	80	100	920	0.1–0.3

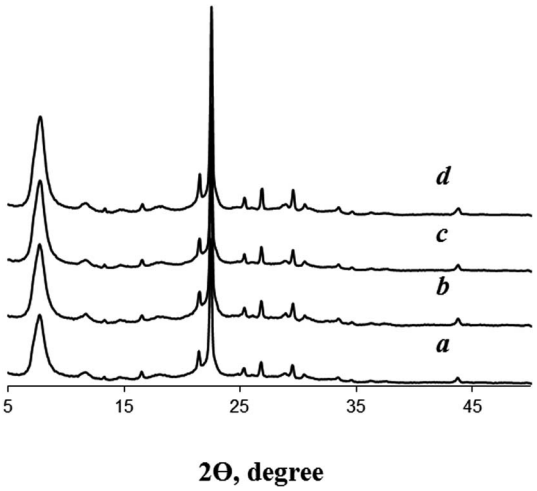

Fig. 2 XRD patterns of synthesized samples: (a) BEA, (b) BEA-s-25, (c) BEA-s-75 and (d) BEA-s-250.

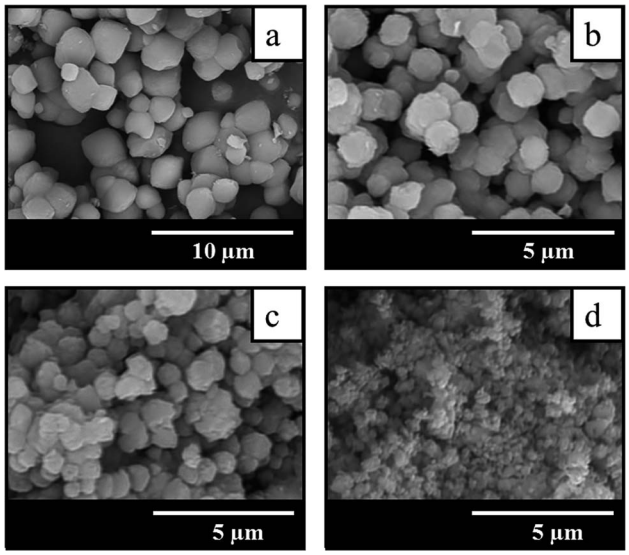

Fig. 3 SEM images of samples prepared by the SAC method in the absence (a) and in the presence of seeds with a different SAR of 25 (b), 75 (c) and 250 (d).

BEA (Fig. S1†). This observation differs from the findings of Cheng *et al.*,[14] who pointed to the formation of zeolite MOR with low crystallinity after crystallization of non-seeded gel of the same composition for 48 h. However, our results definitely confirm that dry gel with $TEAOH/SiO_2 = 0.1$ is rather difficult to crystallize into zeolite BEA in the absence of seeds and that the presence of zeolite seeds is crucial for these conditions.

Table 1 shows that the inorganic yield of all solid products is rather high and SiO_2/Al_2O_3 ratio in synthesized BEA materials is close to SAR in the initial gel, which is typical for the crystallization of dry gel[23,24] and differs from hydrothermal synthesis.[30] However, as can be noted from Table 1, for all the samples the yield is lower than 100% and SAR is lower than in the initial gel. This points to slightly lower incorporation efficiency of silica species with respect to alumina. Most probably, soluble silicate species which were not involved in crystallization are washed out from the dry gel by water vapor during the synthesis or by rinse water during washing procedure. The difference between the samples is not significant however there is a noticeable tendency in decreasing of product yield from 88 to 80% and SAR from 37 to 32 with increasing SAR in seeds (Table 1). This points to significant effect of seeds composition on the crystallization behavior of dry gel.

The comparison of SEM images of crystallization products shown in Fig. 3 suggests that the addition of seeds not only increases the crystallization rate and allows to get highly crystalline BEA zeolites in less time, but also influences the morphology and particle size of the samples obtained. The sample BEA synthesized in the absence of seeds show large and smooth BEA zeolite particles with the size of 1.5–4 μm (Fig. 3a). The addition of seeds results in the decrease of particle size up to 0.2 μm. Among the seeded samples the smallest particles of ~0.2 μm are observed in the case of sample BEA-s-250 (Fig. 3d), whereas the largest particles of 0.7–1.4 μm are found for sample BEA-s-25 (Fig. 3b). The sample BEA-s-75 shows intermediate case with broad particle distribution within 0.3–1.3 μm (Fig. 3c).

It appears that the size of BEA particles in the products does not depend on the crystal size of the seeds used for SSAC but is influenced mainly by their SiO_2/Al_2O_3 ratio. The increase of SAR in seeds from 25 to 250 leads to the decrease of average size of BEA zeolite particles from 1 to 0.2 μm. This effect is presumably due to different dissolution rate of seeds with different SAR in the alkaline media during the gel preparation. Similar tendency was observed in the case of seeded OSDA-free synthesis under hydrothermal conditions.[31] However, in that case the authors observed also the influence of seed crystal size, which was much stronger than the effect of SAR.

Besides SAR, the dissolution of seeds in the alkaline media can be also affected by the presence of defects in the zeolite structure.[32,33] To verify the effect of defects, FT-IR and ^{29}Si MAS NMR data were used (Fig. S3 and S4†). The results show that the amount of SiOH defects is similar in the case of BEA-75 and BEA-250 seeds and lower in the case of BEA-25 (Table S1†). This result suggests that the amount of defects in seeds is not the main factor in our case.

Thus, in our crystallization conditions the key factor which influences the crystal size of the product is the seed SiO_2/Al_2O_3 ratio. Although the seeds used for the synthesis of BEA-s-250 have the largest size (0.4–1.3 μm), they have the lowest stability and the highest rate of dissolution in the alkaline media due to low Al content. This results in higher amount of crystallization nuclei in the gel and therefore smaller particle size in the product. On the contrary, the seeds used for the synthesis BEA-s-25 are much smaller in size (0.1–0.3 μm), but due to high content of Al the dissolution rate in this case is lower, which results in the lesser amount of crystallization nuclei and larger particle size. In the case of BEA-s-75, the size of seeds is the same as in BEA-s-25, but SAR is higher, which leads to smaller BEA particles. High heterogeneity in the size of BEA particles in the latter case could be due to non-uniform

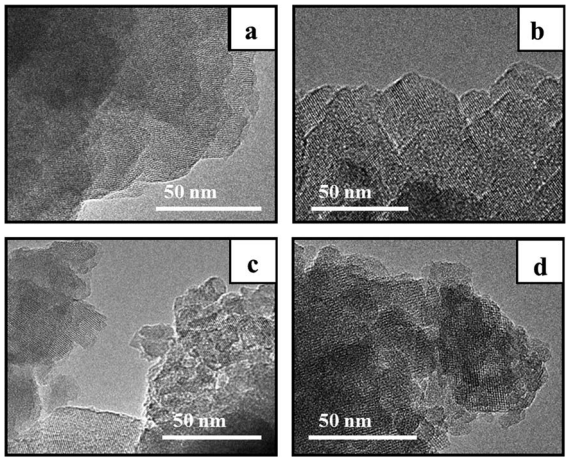

Fig. 4 TEM images of synthesized samples: (a) BEA; (b) BEA-s-25; (c) BEA-s-75 and (d) BEA-s-250.

dissolution of seeds with SiO_2/Al_2O_3 of 75 and formation of nucleation centers with broad distribution in size. Apparently, for the process of BEA zeolite formation by steam-assisted synthesis from the matrix of the dense gel with a low mobility of components, it is very important to have a uniform and homogeneous distribution of nuclei in the matrix of a dense dried precursor-gel.[12]

The TEM images of the synthesized samples reveal that all the BEA particles observed in SEM images are composed of nanocrystallites with uniform size of 5–30 nm but different packing density (Fig. 4).

Samples BEA and BEA-s-25 show polycrystals with ordered intergrown nanocrystallites of 5–30 nm with lattice fringes oriented in the same direction throughout the whole particle. On the contrary, the TEM image of the sample BEA-s-250 reveals hierarchical aggregates of assembled/intergrown nanocrystallites of 5–20 nm with lattice fringes oriented in different directions. The sample BEA-s-75 shows different regions composed of polycrystalline particles with ordered intergrown nanocrystallites and hierarchical aggregates of assembled/intergrown nanocrystallites.

These observations are fully in line with adsorption data shown in Fig. 5. Samples BEA and BEA-s-25 show type I nitrogen adsorption–desorption isotherms, characterized by a significant uptake at low pressure ($P/P_0 < 0.1$) and nearly flat region in the range of $P/P_0 = 0.1$–0.9. A step in the range of $P/P_0 > 0.9$ is due to interparticle adsorption, whereas small inflexion and hysteresis around P/P_0 of 0.45 indicates that polycrystals contain small amount of mesopores with restricted connection to the external surface of polycrystals.

Such isotherms are typical for microporous zeolites with large crystals, which is indeed revealed by SEM images of BEA and BEA-s-25 showing large polycrystals with the size of 1.5–4.0 and 0.7–1.4 μm, respectively (Fig. 3a and b). The pore size distributions in these samples calculated from the desorption branches based on the BJH model (Fig. S2†) shows two peaks: a narrow one at *ca.* 4 nm and a broad one in the range of higher than 10 nm. The former is attributed to the so-called tensile

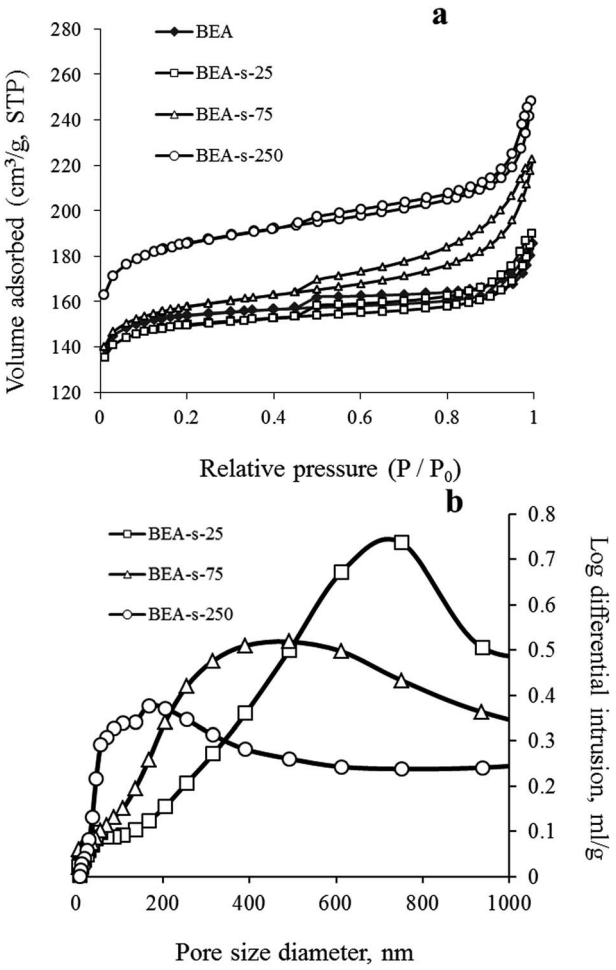

Fig. 5 N_2 adsorption–desorption isotherms (a) and Hg-porosimetry (b) of synthesized BEA zeolites.

strength effect associated with a forced closure of the hysteresis loop which is observed in a sudden drop of volume adsorbed at the $P/P_0 = 0.45$.[34] The latter can be assigned to the adsorption in the interparticle meso- and macropores, which extend beyond the detection range of nitrogen sorption. Application of Hg-porosimetry show that the mean diameter of the pores formed in between BEA polycrystals in sample BEA-s-25 is *ca.* 750 nm (Fig. 5b), which is in line with SEM data (Fig. 3b).

Samples BEA-s-75 and BEA-s-250 show different adsorption–desorption isotherms, characterized by a slope in the range of $P/P_0 = 0.1$–0.9 with a distinct H3 hysteresis loop originating from capillary condensation. Such isotherms correspond to hierarchical micro–mesoporous materials containing both micropores and mesopores. The BJH analysis (desorption branch) reveals very broad distribution of mesopores in the range of 4–100 nm and higher (Fig. S2†). The broadest pore size distribution is observed in the case of BEA-s-75, which is characterized by the broadest size distribution of crystal aggregates (Fig. 3c). These mesopores could be attributed to both intercrystalline pores located in between the nanocrystallites intergrown in BEA aggregates and the pores formed in between BEA aggregates. Hg-porosimetry point that the mean diameters of the pores in

between BEA aggregates of samples BEA-s-75 and BEA-s-250 are *ca.* 490 and 170 nm (Fig. 5b), which corresponds to the size of BEA aggregates determined by SEM (Fig. 3c and d).

Textural properties of the samples, summarized in Table 1, demonstrate that the total pore volume (determined as the volume sorbed at $P/P_0 = 0.95$) and surface area increase in the following range of the samples: BEA < BEA-s-25 < BEA-s-75 < BEA-s-250 due to the increased contribution of mesopores, whereas the micropore volume is the highest in the case of BEA-s-250 (0.24 $cm^3\ g^{-1}$).

To summarize the analysis of the data obtained suggest that the composition of seeds used for dry gel crystallization affect significantly textural and morphological properties of the final products. High aluminum content (SAR = 25) in seeds leads to formation of large polycrystals composed of densely intergrown ordered nanocrystallites with low contribution of intra- and interparticle mesopores. On the contrary, low Al content in seeds (SAR = 250) results in formation of small hierarchical aggregates of assembled/intergrown disordered nanocrystallites with high contribution of intra- and interparticle mesopores. The sample BEA-s-75 shows intermediate case with broad distribution of particles and pores. The observed differences in textural and morphological features suggest that the aluminium content in the seeds affects the mechanism of seeding.

Effect of seeds composition on the mechanism of seeding

There are several hypotheses in the literature on the fate of seeds during hydrothermal synthesis of zeolite BEA and on the mechanism of seeding.[20,31,35,36] Xiao *et al.*[35] proposed core–shell mechanism, according to which BEA seeds introduced during the gel preparation remain intact during the hydrothermal synthesis and provide a surface for crystal growth. Kamimura *et al.*[36] suggested that BEA seeds are partially dissolved and disaggregated into small pieces during the initial step of hydrothermal treatment and the new BEA is crystallized on the surface of these species exposed and/or dispersed in the interface of the amorphous aluminosilicate and the liquid phase. Finally, Zheng *et al.*[31] revealed that both BEA seed residues and the dissolved BEA fragments can serve as the source of nuclei for crystal growth.

To understand the mechanism of seeding in the case of SSAC method and to elucidate the role of BEA seeds with different composition on this mechanism we tried to analyze the fate of different seeds during SSAC. To establish the relationship between the amount of seeds taken for synthesis and the amount of BEA particles (polycrystals or aggregates) in final products we made a simple estimation based on the knowledge of the mean size of crystals in BEA seeds and products determined from SEM images. The detailed description is given in ESI (Table S2†). The results of calculations are presented in Table 2.

The data obtained show that the seed with SAR = 25 and the mean size of crystal of 200 nm produces a single polycrystal with the size of 1000 nm, whereas the seed with SAR = 250 and the size of 1000 nm yields 1×10^4 crystal aggregates with the size of 200 nm. These findings give a hint that the seeds rich in Al do not dissolve during gel preparation and each seed provides a surface for nanocrystals growth *via* core–shell mechanism. The nanocrystallites are therefore grown in the same direction from the surface nuclei, which leads to the formation of polycrystals with densely intergrown nanocrystallites as in the case of membranes.[37,38]

Table 2 Estimated amounts of BEA particles in seeds and products

Sample	N_s[a]	N_p[b]	N_p/N_s
BEA-s-25	2.5×10^{12}	2.1×10^{12}	0.8
BEA-s-250	2.0×10^{10}	2.4×10^{14}	1.2×10^4

[a] N_s – amount of BEA crystals in seeds taken for the synthesis. [b] N_p – amount of BEA crystals (polycrystals or aggregates) in the products obtained.

On the contrary, Si-rich seeds (SAR = 250) dissolve into tiny fragments which are homogeneously dispersed in the gel during its preparation. During the crystallization, these tiny fragments serve as individual nuclei for BEA crystallization, which lead to the formation of BEA nanocrystallites grown in different directions and formation of hierarchical materials with two types of mesopores: in between nanocrystallites inside BEA aggregates and in between aggregates of nanocrystallites.

In the sample BEA-s-75, the particle size distribution in the product is very broad and accurate estimations cannot be done, however this sample obviously shows an intermediate case since the product contains both polycrystals with densely intergrown nanocrystallites with bigger size and aggregates of nanocrystallites with smaller size (Fig. 4c). Operation of two different mechanisms explains very broad distribution of BEA particles in this case (Fig. 3c).

The mechanism proposal presented in Fig. 6 rationalizes further all the above observations. During the gel preparation, the seeds are subjected to strong alkaline media, which leads to their partial dissolution. The degree of dissolution depends on SiO_2/Al_2O_3 in the seeds. The Si–O–Al bonds are rather stable for hydrolysis in alkaline media compared to Si–O–Si bonds, which are easily hydrolyzed. Therefore, the seeds with high density of framework Al sites (SAR = 25) are practically inert to dissolution, as most of the Si atoms are stabilized by neighboring Al. On the contrary, the seeds with high density of Si atoms (SAR = 250) undergo substantial dissolution and formation of numerous zeolitic fragments, homogeneously dispersed in the gel. The seeds with intermediate SAR = 75 may lead to both large seeds residues and small zeolitic fragments.

During the crystallization step the intact seeds, residual seeds and tiny zeolitic fragments are involved in nucleation. Large zeolitic seeds and seeds residues provide for large number of nuclei on their surface, which initiates dense oriented crystal growth leading to the formation of polycrystals with ordered intergrown nanocrystallites, showing lattice fringes oriented in the same direction throughout the whole particle (Fig. 4b). Small zeolitic fragments provide for individual dispersed nuclei, which are converted during crystallization

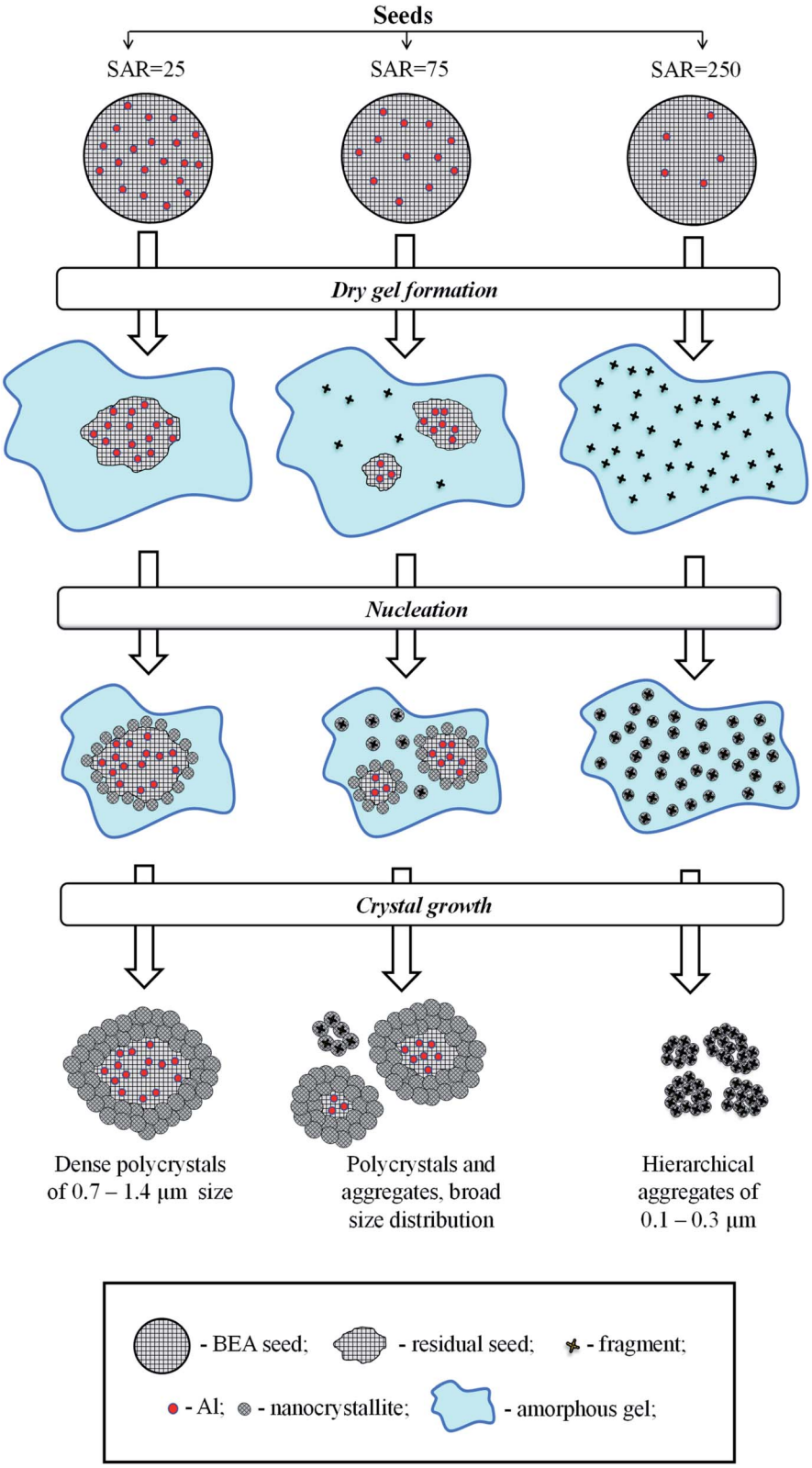

Fig. 6 Mechanism of seeding.

into tiny isolated nanocrystallites, which further rearrange into hierarchical aggregates *via* condensation at contact points of their surfaces (Fig. 4d). This aggregation creates the intercrystalline mesoporosity. The presence of both residual seeds and tiny zeolitic fragments in the gel of sample BEA-s-75 leads to the formation of both polycrystalline particles with ordered intergrown nanocrystallites and hierarchical aggregates of

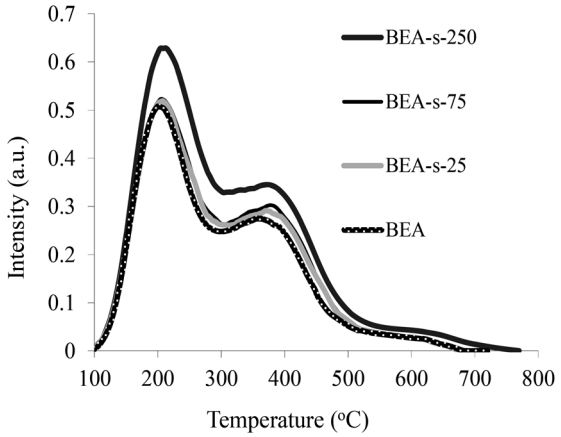

Fig. 7 NH_3-TPD curves of synthesized BEA zeolites.

assembled/intergrown nanocrystallites and results in very broad particle size distribution.

Acidic properties

The acidic properties of the samples obtained were studied by the NH_3 TPD method (Fig. 7). The NH_3 TPD profiles for all the samples show two pronounced peaks indicating the presence of two types of acid sites in BEA zeolites, *i.e.*, weak acid sites characterized by the peak at 200 °C and strong acid sites showing the peak at 380–400 °C. The quantification of the NH_3 TPD data presented in Table 1 point that the content of acid sites is very similar for samples BEA, BEA-s-25 and BEA-s-75 (*ca.* 800 mmol g^{-1}), whereas in the case of the sample BEA-s-250 this value is slightly higher and amounts to 920 mmol g^{-1}.

This observation can be due to both a lower SiO_2/Al_2O_3 ratio in this product and/or its higher crystallinity. Thus, our results demonstrate that steam assisted conversion with variable seed composition allows to obtain BEA zeolites with different crystal size and morphology but similar chemical composition and acid properties.

Catalytic evaluation in benzene alkylation with propylene

The catalytic properties of the samples with different morphology and particle size and similar acidity were studied in liquid-phase alkylation of benzene with propylene under 3 MPa and at 170 °C. High propene weight hourly space velocity ($WHSV_{propylene}$ = 52 h^{-1}) was used to observe the difference between the catalysts. Two sets of experiments with benzene/propylene (B/P) molar ratio of 10/1 and 5/1 were carried out to compare the catalysts activity and stability with time on stream. The main products observed in both sets of experiments involved cumene, diisopropylbenzenes (DIPB) and trace amounts of triisopropylbenzenes (TIPB) and *n*-propylbenzene (NPB). Besides that, small amounts of other products were observed including propylene oligomers, fragmentation products and *etc.* The results are depicted in Fig. 8 and Table 3.

At higher B/P molar ratio of 10, the conversion is more stable with TOS, which allows to compare the activity of various catalysts. The results (Fig. 8a) show that all the catalysts

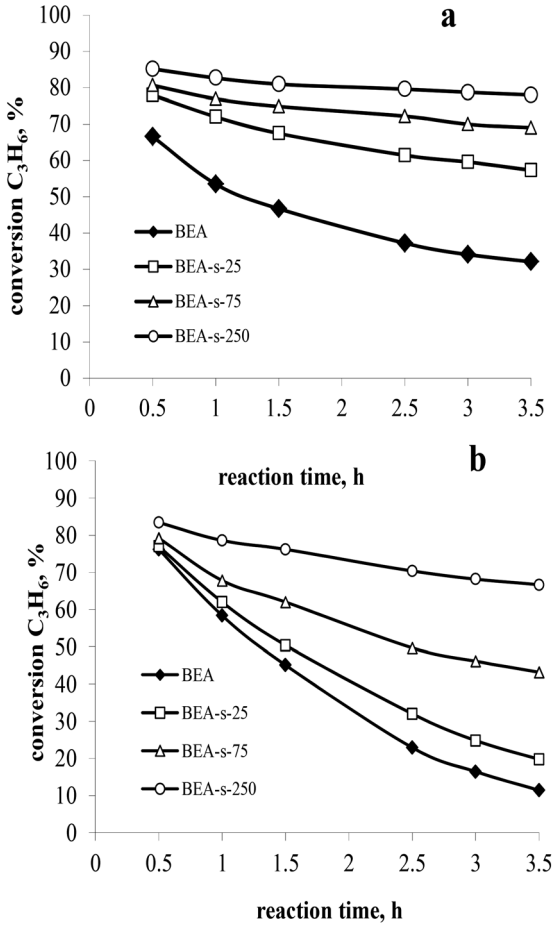

Fig. 8 Propylene conversion *versus* time on stream at 3 MPa, 170 °C, $WHSV_{propylene}$ = 52 h^{-1} and B/P molar ratio of 10 (a) and 5 (b).

obtained with seeds are more active than those synthesized without seeds. Among the seeded catalysts, the following range of activity is observed: BEA-s-250 > BEA-s-75 > BEA-s-25. Sample BEA-s-250 involving hierarchical aggregates with small size (100–300 nm) demonstrates the highest catalytic activity. On the contrary, polycrystalline BEA-s-25 with large particle size (0.7–1.4 μm) shows the lowest propene conversion. It should be mentioned that the order of activity also correlates with SiO_2/Al_2O_3 ratio and the content of acid sites in the samples. However, according to ref. 29, these rather modest differences in composition could hardly explain the significant difference in activity, which is most probably related to the size and morphology of BEA particles.

The analysis of product distribution (Table 3) points to the increase of the content of bulky DIPB and TIPB products of alkylation on the expense of cumene in the same range of catalysts. These bulky products are most probably formed on the external surface and in the pre-surface layer of BEA particles or in the intercrystallite mesopores of BEA aggregates.[39] The increase of the external surface area and the intercrystallite mesoporosity in the following range of catalysts BEA-s-250 > BEA-s-75 > BEA-s-25, thus explains the observed differences in activity and selectivity.

Table 3 Evaluation of BEA samples in benzene alkylation with propylene at different B/P molar ratio (170 °C, 3 MPa, $WHSV_{propylene} = 52\ h^{-1}$, 3.5 h of reaction)

	$C_6H_6/C_3H_6 = 5$				$C_6H_6/C_3H_6 = 10$			
Process parameters	BEA	BEA-s-25	BEA-s-75	BEA-s-250	BEA	BEA-s-25	BEA-s-75	BEA-s-250
Conversion of C_3H_6, %[a]	76.2	77.0	79.2	83.4	66.6	78.0	80.7	85.2
Product selectivity, wt%								
Cumene	88.2	88.0	86.1	85.1	93.1	92.4	92.3	92.2
DIPB	11.2	11.4	13.2	14.2	6.5	7.3	7.4	7.5
TIPB	0.04	0.05	0.14	0.19	0.02	0.03	0.03	0.05
n-Propylbenzene	0.04	0.04	0.04	0.04	0.03	0.03	0.03	0.03
Other products	0.52	0.51	0.52	0.47	0.35	0.24	0.24	0.22

[a] Maximum prolylene coversion achieved.

To conclude, the small size of BEA zeolite aggregates and the presence of intra- and interparticle mesopores improve the accessibility of acidic sites and facilitate the mass transfer, which contributes to more efficient diffusion of reagents and reaction products from acidic sites of the catalyst and accounts for higher activity and deeper alkylation into DIPB and TIPB.

The catalyst deactivation is more pronounced in the set of experiments with B/P molar ratio of 5 (Fig. 8b), which is caused by significant contribution of propylene oligomerization at the higher propylene content in the reaction mixture and formation of heavier products. This is consistent with the literature data.[27]

The highest rate of deactivation observed in the case of samples BEA and BEA-s-25 can be ascribed to diffusion limitations in large polycrystals, which prevents the desorption of the products from the catalyst and favours secondary reactions leading to heavy carbonaceous deposits blocking the catalyst porous system. The formation of hierarchical aggregates with smaller particle size in the case of sample BEA-s-250 facilitates the diffusion of reaction products and reduces the deactivation rate of the catalyst leading to higher stability with time on stream.

The best catalyst performance in terms of activity and stability was observed over BEA-s-250 catalyst. This catalyst shows the highest activity and resistance to deactivation. Therefore it was tested under the conditions close to industrial operation of zeolite catalysts in benzene alkylation with propene: 3 MPa, 170 °C, $WHSV_{propylene} = 2.4\ h^{-1}$, B/P = 5/1 (Fig. 9). The results show that the sample provides for 100% conversion of propene, the selectivity to alkylation products (cumene + DIPB + TIPB) of 99.7 wt%, and a cumene selectivity of 86.7 wt% within 10 h of testing.

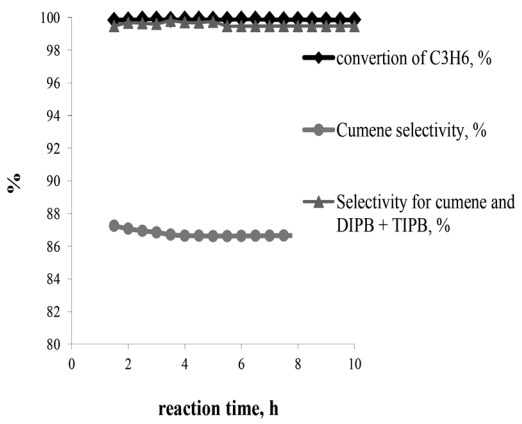

Fig. 9 Benzene alkylation with propene over BEA-s-250.

Conclusions

It is demonstrated that by variation BEA seeds composition during SSAC it is possible to change the size of BEA particles from several microns to hundred nanometers and to modify their morphology from polycrystalline BEA particles with densely intergrown nanocrystallites to hierarchical aggregates of nanocrystallites with high intercrystalline mesoporosity. The seeds with SiO_2/Al_2O_3 of 25 give large polycrystalline BEA particles with mean size of 1.0 μm. On the contrary, the seeds with SiO_2/Al_2O_3 of 250 yield small hierarchical aggregates with mean size of 200 nm. The seeds with intermediate SiO_2/Al_2O_3 of 75 provide for both polycrystals and aggregates with broad particle size distribution within 0.3–1.3 μm.

The results suggest that the composition of seeds determines the mechanism of seeding. Al-rich seeds provide for core–shell mechanism involving the nucleation and crystal growth on the external surface of the intact particles of parent seeds and leading to the formation of core–shell particle of product with the initial seed in the core and the dense intergrown nanocrystallites in the shell. Si-rich seeds obey dissolution mechanism including dissolution and disaggregation of the initial seeds and formation of tiny zeolitic fragments, which serve as individual nuclei for the formation of numerous tiny isolated nanocrystallites aggregating in hierarchical particles.

The evaluation of BEA catalysts with different particle size and morphology in benzene alkylation with propene revealed that the decrease of particle size and formation of intercrystalline mesoporosity in hierarchical aggregates leads to the significant improvement of catalytic activity and reduces the deactivation resulting in higher stability with time on stream in cumene synthesis. The effect is due to the improvement of the

acidic sites accessibility and the transport of reaction products. The best catalyst performance in terms of activity and stability was observed over BEA catalyst obtained from Si-rich seeds (SAR = 250), which showed 100% conversion of propene, 99.7 wt% selectivity to alkylation products and the highest stability with time on stream.

Conflicts of interest

There are no conflicts to declare.

Acknowledgements

This work was carried out within the State Program of TIPS RAS.

References

1 W. Vermeiren and J. P. Gilson, *Top. Catal.*, 2009, **52**, 1131–1161.
2 G. Bellussi, G. Pazzuconi, C. Perego, G. Girotti and G. Terzoni, *J. Catal.*, 1995, **157**, 227–234.
3 O. V. Shutkina, O. A. Ponomareva and I. I. Ivanova, *Catal. Ind.*, 2015, **7**, 282–286.
4 B. O. Dalla Costa and C. A. Querini, *Appl. Catal., A*, 2010, **385**, 144–152.
5 R. Pradhan and B. S. Rao, *Appl. Catal., A*, 1993, **106**, 143–153.
6 M. Casagrande, L. Storaro, M. Lenarda and R. Ganzerla, *Appl. Catal., A*, 2000, **201**, 263–270.
7 R. Nakao, Y. Kubota, N. Katada, N. Nishiyama, K. Kunimori and K. Tomishige, *Appl. Catal., A*, 2004, **273**, 63–73.
8 T. Tabata, H. Ohtsuka, L. M. F. Sabatino and G. Bellussi, *Microporous Mesoporous Mater.*, 1998, **21**, 517–524.
9 H. Y. Luo, J. D. Lewis and Y. Román-Leshkov, *Annu. Rev. Chem. Biomol. Eng.*, 2016, **7**, 663–692.
10 R. Mostowicz, F. Testa, F. Crea, R. Aiello, A. Fonseca and J. B. Nagy, *Zeolites*, 1997, **18**, 308–324.
11 A. Petushkov, G. Merilis and S. C. Larsen, *Microporous Mesoporous Mater.*, 2011, **143**, 97–103.
12 S. Mintova, V. Valtchev, T. Onfroy, C. Marichal, H. Knözinger and T. Bein, *Microporous Mesoporous Mater.*, 2006, **90**, 237–245.
13 K. Möller, B. Yilmaz, R. M. Jacubinas, U. Müller and T. Bein, *J. Am. Chem. Soc.*, 2011, **133**, 5284–5295.
14 X. Cheng, J. Mao, X. Lv, T. Hua, X. Cheng, Y. Long and Y. Tang, *J. Mat. Chem. A.*, 2014, **2**, 1247–1251.
15 M. A. Camblor and J. Pérez-Pariente, *Zeolites*, 1991, **11**, 202–210.
16 J. Perez-Pariente, J. A. Martens and P. A. Jacobs, *Appl. Catal.*, 1987, **31**, 35–64.
17 B. Xie, J. Song, L. Ren, Y. Ji, J. Li and F. S. Xiao, *Chem. Mater.*, 2008, **20**, 4533–4535.
18 G. Majano, A. Darwiche, S. Mintova and V. Valtchev, *Ind. Eng. Chem. Res.*, 2009, **48**, 7084–7091.
19 Y. Kamimura, W. Chaikittisilp, K. Itabashi, A. Shimojima and T. Okubo, *Chem.–Asian J.*, 2010, **5**, 2182–2191.
20 K. Iyoki, K. Itabashi and T. Okubo, *Microporous Mesoporous Mater.*, 2014, **189**, 22–30.
21 G. Majano, L. Delmotte, V. Valtchev and S. Mintova, *Chem. Mater.*, 2009, **21**, 4184–4191.
22 P. R. H. Prasad Rao and M. Matsukata, *Chem. Commun.*, 1996, **12**, 1441–1442.
23 M. Matsukata, T. Osaki, M. Ogura and E. Kikuchi, *Microporous Mesoporous Mater.*, 2002, **56**, 1–10.
24 P. R. H. Prasad Rao, C. L. y. Leon, K. Ueyama and M. Matsukata, *Microporous Mesoporous Mater.*, 1998, **21**, 305–313.
25 M. Matsukata, M. Ogura, T. Osaki, E. Kikuchi and A. Mitra, *Microporous Mesoporous Mater.*, 2001, **48**, 23–29.
26 V. Smirnov, B. V. Romanovsky, I. I. Ivanova, E. G. Derouane and Z. Gabelica, *Stud. Surf. Sci. Catal.*, 1994, **84**, 1797–1804.
27 G. Bellussi, G. Pazzuconi, C. Perego, G. Girotti and G. Terzoni, *J. Catal.*, 1995, **157**, 227–234.
28 S. Siffert, L. Gaillard and B. L. Su, *J. Mol. Catal. A: Chem.*, 2000, **153**, 267–279.
29 T. O. Bok, E. P. Andriako, D. O. Bachurina, E. E. Knyazeva and I. I. Ivanova, *Pet. Chem.*, 2019, **59**, 1320–1325.
30 T. O. Bok, E. D. Onuchin, A. V. Zabil'skaya, S. V. Konnov, E. E. Knyazeva, A. V. Panov, A. V. Kleimenov and I. I. Ivanova, *Pet. Chem.*, 2016, **56**, 1160–1167.
31 Y. Wan Zheng, W. Yang, F. Ling, H. Xie, X. Fang and H. Guo, *Chin. J. Catal.*, 2014, **35**, 1800–1810.
32 D. Fodor, A. Beloqui Redondo, F. Krumeich and J. A. van Bokhoven, *J. Phys. Chem. C*, 2015, **119**, 5447–5453.
33 T. Li, J. Ihli, Z. Ma, F. Krumeich and J. A. van Bokhoven, *J. Phys. Chem. C*, 2019, **123**(14), 8793–8801.
34 M. Thommes, *Nanoporous Materials: Science and Engineering*, 2004, pp. 317–364.
35 B. Xie, H. Zhang, C. Yang, S. Liu, L. Ren, L. Zhang, X. Meng, B. Yilmaz, U. Müller and F. S. Xiao, *Chem. Commun.*, 2011, **47**, 3945–3947.
36 Y. Kamimura, S. Tanahashi, K. Itabashi, A. Sugawara, T. Wakihara, A. Shimojima and T. Okubo, *J. Phys. Chem. C*, 2011, **115**, 744–750.
37 O. De La Iglesia, V. Sebastián, R. Mallada, G. Nikolaidis, J. Coronas, G. Kolb, R. Zapf, V. Hessel and J. Santamaría, *Catal. Today*, 2007, **125**, 2–10.
38 K. Shen, W. Qian, N. Wang, C. Su and F. Wei, *J. Am. Chem. Soc.*, 2013, **135**, 15322–15325.
39 G. Popov, V. S. Pavlov and I. I. Ivanova, *J. Catal.*, 2016, **335**, 155–164.

